Design and Validation of a Torso-Dynamics Estimation System (TES) for Hands-Free Physical Human-Robot Interaction*

Seung Yun Song, *Student Member, IEEE*, Yixiang Guo, Chentai Yuan, Nadja Marin, Chenzhang Xiao, Adam Bleakney, Jeannette Elliott, Joao Ramos, *Member, IEEE*, Elizabeth T. Hsiao-Wecksler, *Member, IEEE*

Abstract— We designed and validated two interfaces for physical human-robot interaction that utilize torso motions for hands-free navigation control of riding or remote mobile robots. The Torso-dynamics Estimation System (TES), which consisted of an instrumented seat (Force Sensing Seat, FSS) and a wearable sensor (inertial measurement unit, IMU), was developed to quantify the translational and rotational motions of the torso, respectively. The FSS was constructed from six uniaxial loadcells to output 3D resultant forces and torques, which were used to compute the translational movement of the 2D center of pressure (COP) under the seated user. Two versions of the FSS (Gen 1.0 and 2.0) with different loadcell layouts, materials, and manufacturing methods were developed to showcase the versatility of the FSS design and construction. Both FSS versions utilized low-cost components and a simple calibration protocol to correct for dimensional inaccuracies. The IMU, attached on the user's upper chest, used a proprietary algorithm to compute the 3D torso angles without relying heavily on magnetometers to minimize errors from electromagnetic noises. A validation study was performed on eight test subjects (six able-bodied users and two manual wheelchair users with reduced torso range of motion) to validate TES estimations by comparing them to data collected on a research-grade force plate and motion capture system. TES readings displayed high accuracy (average RMSE of 3D forces, 3D torques, 2D COP, and torso angles were well less than maximum limits of 5N, 5Nm, 10mm, and 6°, respectively).

I. INTRODUCTION

Estimations of torso motions of seated users are essential in physical human-robot interaction (pHRIs) that incorporate hands-free (HF) control for navigating riding or remote mobile robots (e.g., [1]–[8]). Force resistive sensors or research-grade pressure mats have been used for directly navigating personal mobility devices, such as two-wheeled self-balancing devices or electrically powered wheelchairs [1], [4]. Inertial measurement units (IMUs) have also been placed on the shoulders of powered wheelchair users to detect and measure small upper body movements, which were mapped to control the wheelchair's speed and direction [2]. Sensors estimating torso angles, torso induced forces, or trunk

*Research supported by National Science Foundation National Robotics Initiative (award number 2024905).

S. Y. Song, Y. Guo, C. Yuan, N. Marin, C. Xiao, J. Ramos, and E. T. Hsiao-Wecksler are with Dept of Mechanical Science and Engineering at the University of Illinois at Urbana-Champaign (UIUC), IL 61801 USA (phone: 1-217-333-3415; e-mail: ethw@illinois.edu). A. Bleakney and J. Elliott are with Division of Disability Resources and Educational Services at UIUC. Y. Guo and C. Yuan contributed equally and are also with School of Mechanical Engineering, Zhejiang University, Hangzhou 310027, China. C. Xiao is now with Intuitive, CA, USA. J. Ramos is also with Boston Dynamics, MA, USA.

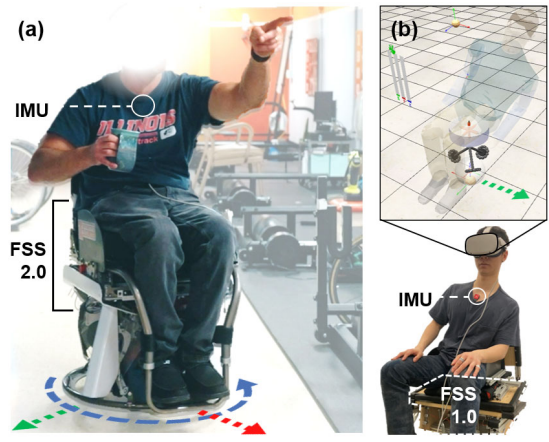


Figure 1. Applications of the Torso-dynamics Estimation System (TES), which consists of the Force Sensing Seat (FSS) and IMU: (a) physical or (b) virtual human-robot interface controlling an omnidirectional personal mobility device, i.e., Personalized Unique Rolling Experience (PURE).

muscle EMG signals have been utilized as HF pHRIs for remotely controlled mobile robots such as aerial drones [3], [5], [6]. However, these sensor systems have several drawbacks that limit their practical application.

The sensors used in these previous studies were costly, bulky, heavy, difficult to customize, and/or did not comprehensively estimate torso mechanics. While research grade pressure mats provide portability and accurate measurement of pressure distribution [1], [4], these mats can be expensive. Although research grade force plates offer highly accurate force, torque, and center of pressure (COP) measurements [3], these plates can be bulky and heavy. Lastly, these sensors estimate only a limited number of kinetic or kinematic signals related to torso mechanics. For example, some studies only relied on kinematic signals when analyzing the torso motions of the seated user [2]. Access to a more comprehensive dataset quantifying torso motions could offer multidimensional understanding for different applications. For example, studies aiming to detect postures of seated users using data-driven methods could utilize not only body pressure distribution data, but also kinetic signals (i.e., contact forces at the seat) as well as kinematic signals (i.e., torso lean angles) to enhance accuracy of posture detection models [3], [5].

Our group is currently developing a novel self-balancing omnidirectional personal mobility device that can translate forward, backward, sideways, and rotate about a fixed vertical axis (Figure 1). We call the device PURE, which stands for Personalized Unique Rolling Experience. The vision of PURE is to create a compact and lightweight ridable robot that has a footprint approximately as wide as the rider's hips and

can be easily disassembled for transportation in a vehicle. PURE can be navigated with control signals generated uniquely using an intuitive HF control based on torso motions. The HF control uses torso kinetic and kinematic signals that are scaled according to the rider's preference and used as target values for PURE's balancing controller.

In this paper, we present the development of two versions of a compact, lightweight, accurate, and versatile Torsodynamics Estimation System (TES) that can estimate kinetic and kinematic signals related to torso motions of seated users in real time (Figure 2). In the current embodiment, the TES estimated torso kinetics using a custom Force Sensing Seat (FSS) and torso rotational kinematics using a commercially available inertial measurement unit (IMU). Human subject tests were conducted to validate the accuracy of the proposed sensor system by comparing the readings of the FSS and IMU to gold standard equipment using a research-grade force plate and motion capture system. The TES design and construction are described in detail to allow others to replicate and customize the TES to their application accordingly.

II. METHODS

A. TES Design

The purpose of the TES was to quantify the torso motions of the user in terms of kinetic and kinematic signals in real-time to comfortably navigate PURE using torso-based and HF control. To provide a practical solution for pHRI developers, the TES aimed for minimizing weight while maximizing its compactness, versatility in design and manufacturing methods, robustness to fabrication errors, and cost-effectiveness.

1) Force Sensing Seat (FSS)

The core design principle was to construct a portable, light, and compact force plate that could output the resultant applied forces and torques and location of the center of

Torso-dynamics Estimation System

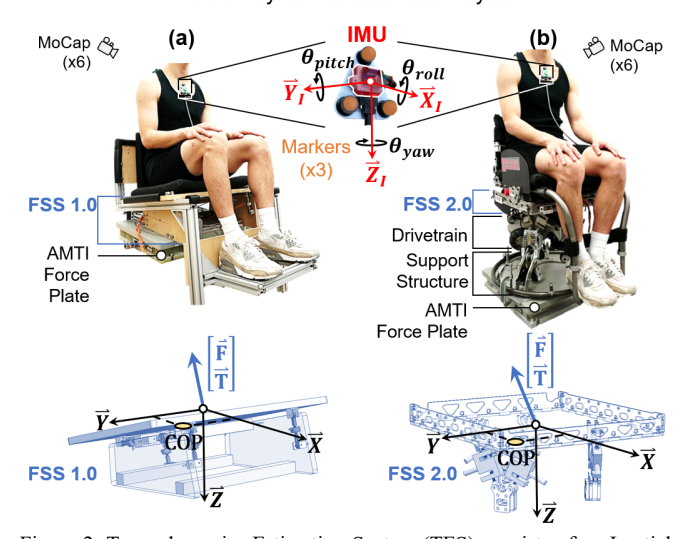


Figure 2. Torso-dynamics Estimation System (TES) consists of an Inertial Measurement Unit (IMU) to estimate 3D torso angles $(\theta_{yaw}, \theta_{pitch}, \theta_{roll})$ and a Force Sensing Seat (FSS) to estimate 3D resultant forces $(\vec{\mathbf{F}})$ and torques $(\vec{\mathbf{T}})$, and 2D COP (COP_x, COP_y) . Two versions of the FSS (Gen 1.0 (a), Gen 2.0 (b)) were developed and validated using research-grade AMTI force plate and Qualisys motion capture (MoCap) system.

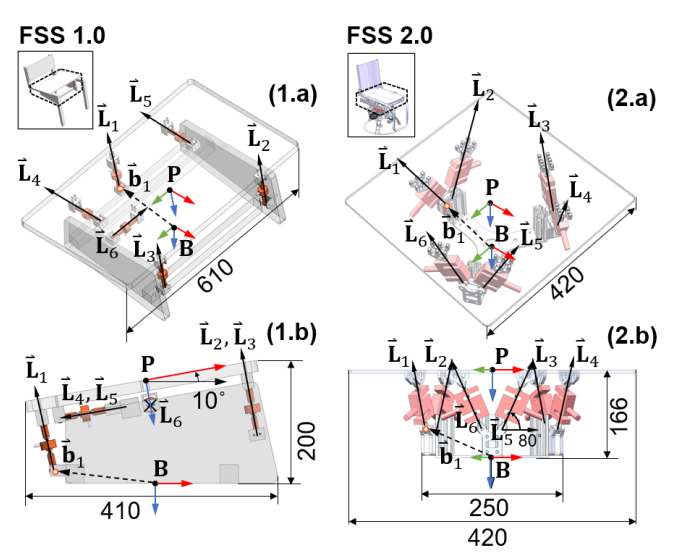


Figure 3. Final loadcell arrangement for FSS Gen 1.0 and Gen 2.0 from (1.a, 2.a) isometric view and (1.b, 2.b) side view. The loadcells $(\vec{\mathbf{L}}_1 - \vec{\mathbf{L}}_6)$ are arranged orthogonally (Gen 1.0) or in a Stewart platform configuration (Gen 2.0). The position vector pointing from the global origin, B, to loadcell #1 $(\vec{\mathbf{b}}_1)$ is shown, and other position vectors are omitted for clarity. The length units are in mm, and red, green, blue arrows are $\vec{\mathbf{x}}, \vec{\mathbf{y}}, \vec{\mathbf{z}}$, respectively.

pressure on the seat. More specifically, the 3D forces ($\vec{\mathbf{F}} = \begin{bmatrix} \vec{\mathbf{F}}_x \ \vec{\mathbf{F}}_y \ \vec{\mathbf{F}}_z \end{bmatrix}^T$) and torques ($\vec{\mathbf{T}} = \begin{bmatrix} \vec{\mathbf{T}}_x \ \vec{\mathbf{T}}_y \ \vec{\mathbf{T}}_z \end{bmatrix}^T$) (i.e., wrench ($\vec{\mathbf{W}} = \begin{bmatrix} \vec{\mathbf{F}}, \vec{\mathbf{T}} \end{bmatrix}^T$)) and 2D center of pressure ($\vec{\mathbf{COP}} = \begin{bmatrix} COP_x \ COP_y \end{bmatrix}^T$). Here, we briefly explain the mathematical derivation for estimating kinetic signals. More details and code for computing $\vec{\mathbf{W}}$ and $\vec{\mathbf{COP}}$ are explained online^a.

In general, this force plate consisted of a floating rigid body (i.e., plate) which was constrained in six degrees-of-freedom by six legs with respect to a fixed rigid body (i.e., base). Each leg contained a uniaxial loadcell with two spherical joints at both ends such that each leg was a two-force member in which the axial loads were measured. $\overrightarrow{\mathbf{W}}$ applied on the FSS plate are transmitted through the six legs axially and are in static equilibrium with the six axial forces $(\vec{\mathbf{L}}_i, i = \{1,2, ... 6\})$ (Figure 3) (1).

$$\vec{\mathbf{W}} = \mathbf{H} \begin{bmatrix} f_1 \\ \vdots \\ f_6 \end{bmatrix} = \begin{bmatrix} \hat{\mathbf{u}}_1 & \dots & \hat{\mathbf{u}}_6 \\ \hat{\mathbf{b}}_1 \times \hat{\mathbf{u}}_1 & \dots & \hat{\mathbf{b}}_6 \times \hat{\mathbf{u}}_6 \end{bmatrix} \begin{bmatrix} f_1 \\ \vdots \\ f_6 \end{bmatrix}$$
(1)

where $\vec{\mathbf{b}}_i$ is the position vector from the origin of base frame \mathbf{B} to the connection point of the i^{th} leg at the base (Figure 3). Each $\vec{\mathbf{L}}_i$ are computed from the corresponding loadcell readings (f_i) and the unit vector $(\hat{\mathbf{u}}_i)$ along leg i as defined in the global coordinate frame of the FSS. $\vec{\mathbf{W}}$ applied on the plate frame \mathbf{P} can be calculated by multiplying a force transformation matrix \mathbf{H} to the six load cell readings (f_i) (2). Note that calibration of $^a\mathbf{H}$ is needed to compensate for manufacturing and assembly errors of the FSS. Then, $\vec{\mathbf{COP}}$ are computed from $\vec{\mathbf{W}}$ [9].

The design goal of the FSS was to estimate these kinetic signals, while satisfying the desired load capacities and with high accuracies. Efforts were made to use commercially available and cost-effective key components for the FSS to provide a practical solution for developers. Since the study's main application was to develop a TES for PURE, i.e., a novel mobility device, there were no previously available load data describing the possible contact forces and torques experienced by the FSS for PURE's application. This made the FSS design process challenging due to the difficulty of setting clear and quantitative design specifications such as load capacities. Thus, the target load estimation specifications for the FSS (Table 1) were determined by first collecting preliminary force data of a single subject (~80kg, current maximum allowable rider's mass on PURE) executing various torso movements (Figure 4).

From these preliminary data, the absolute maximum values of kinetic signals were determined. To define the desired load capacities, a safety factor of 2 was applied to mitigate overloading the loadcells from high impact loads (e.g., impact during transfer into seat) or dynamic loads (e.g., tilting and acceleration of PURE). To set the desired accuracies, a maximum allowable error of 5% was chosen since it matched reported errors of similar sensor systems that estimated contact forces and torques for pHRI purposes (e.g., Nintendo Wii Balance BoardTM [7], [8]). The target load capacities and accuracies were anisotropic since the measured loads were different for each direction. For example, leaning in the sagittal plane generated higher torque than leaning in the frontal plane, since users displayed more range of motion when leaning forward than leaning sideway. The normal force along the vertical axis (i.e., $\bar{\mathbf{F}}_z$) was significantly higher than shear forces on the seat (i.e., forward-backward $\vec{\mathbf{F}}_{\mathbf{x}}$ and leftright $\vec{\mathbf{F}}_{\mathbf{v}}$ directions). These desired load specifications dictated the selection of the loadcell type, loadcell arrangements, and overall FSS structure.

Other design goals of the FSS were satisfying requirements of compact size, lightweight, versatile form factor, versatile choice of manufacturing, and estimation correction for tolerance errors. Two versions (Gen 1.0 and Gen 2.0) sharing the same design principles but different embodiments (e.g., layout and type of loadcells, manufacturing methods) were developed to highlight the versatility in the design space and robustness to fabrication errors (Figure 3). FSS Gen 1.0 (target size (mm): $410 \times 610 \times 200$, target mass (kg): 11) was used for navigating a simulated PURE device in a virtual reality environment, while the physical PURE drivetrain hardware was being developed. FSS Gen 2.0 (target size (mm): $420 \times 420 \times 165$, target mass (kg): 5) was used as part of the pHRI directly mounted on PURE's drivetrain.

TABLE 1. DESIRED LOAD ESTIMATION SPECIFICATIONS FOR FSS GEN 1.0 & 2.0

125 021, 110 00 210										
	$\vec{\mathbf{F}}_{\mathbf{x}}$	$\vec{\mathbf{F}}_{\mathrm{v}}$	$\vec{\mathbf{F}}_{\mathbf{z}}$	\vec{T}_{x}	\vec{T}_{v}	$\overrightarrow{\mathbf{T}}_{\mathrm{z}}$	$COP_{\rm x}$	COP_{y}		
	(N)	(N)	(N)	(Nm)	(Nm)	(Nm)	(mm)	(mm)		
Capacity ^a	200	200	1600	200	400	40	400	200		
Accuracy ^b	5	5	40	5	5	1	10	5		

^aThese capacities contain a factor of safety of 2. ^bQuantified using root-mean-squared-error (RMSE).

a) Versatile FSS Design to Achieve Design Requirements

Versatility of FSS design is critical to satisfy the strict spatial requirements for PURE and for other applications that require different requirements. These spatial requirements may include physical size constraints and form factors. Thus, the FSS utilized six loadcells strategically arranged in parallel configurations for versatility in FSS design (Figure 3) [10]-[14]. The FSS Gen 1.0 required a sufficiently large footprint to accommodate users with various physiques (Fig 3(a)). The FSS Gen 2.0 imposed many dimensional requirements (Figure 3(b)) since it was mounted on PURE's drivetrain (Figure 2,3). Thus, the FSS Gen 2.0 needed to be 1) physically compact to ensure that the overall device's dimensions were similar to if not smaller than a typical manual wheelchair, 2) efficiently packaged with other components (e.g., drivetrain, electronics), and 3) easily accessible for maintenance and repairs.

For the FSS Gen 1.0, three legs were mounted normal to the vertical (z-axis) plane of the plate while the other three were placed on the horizontal (x, y) plane (Figure 3). This configuration allowed for intuitive inspection of the sensor readings since the loadcells were parallel to the coordinate axes of the plate. For example, we can expect a non-zero reading for the 4^{th} and 5^{th} load cells, i.e., \vec{L}_4 , \vec{L}_5 (and near-zero readings for \vec{L}_1 , \vec{L}_2 , \vec{L}_3 , \vec{L}_6) if an external load along the x-axis was applied on the plate.

The FSS Gen 2.0 had all six legs arranged in the semi-regular hexagonal structure of a Stewart Platform (Figure 3). The semi-regular hexagonal structure and symmetrically arranged legs allowed the FSS estimations to be more isotropic (i.e., sensors equally sensitive to all directions) for a given wrench. The plate dimensions were larger than the base since the plate had to hold many critical components such as the seat, electronics, and batteries. The connection points for the plate were further spread out from the center axis than for the base to better accommodate the form factor of PURE (i.e., hourglass shape - wide top due to the seat, slim middle due to compact drivetrain, and wide bottom due to the support structure).

Another benefit of the versatile leg arrangements was that the load sensing behaviors could be customized to fit PURE's load sensing requirements (Table I). By varying the orientation and position of the legs, the force transformation matrix **H** could be altered, enabling us to change the load capacity and sensitivity for sensing forces and torques in different axes for our needs. The appropriate leg configurations for the FSSs were first determined using the desirable load capacities for each axis. The desirable load sensitivities were not defined for the FSSs because the FSS estimations were sensitive enough for PURE's application for almost any given leg arrangements and loadcells, and the load capacities took higher priority than sensitivities since safety was a more critical factor.

Other design changes could be made to the leg design and arrangements to adjust the loading behavior of an FSS. For legs arranged orthogonally to the base frame (e.g., Gen 1.0), increasing the number of legs along the loaded direction or simply selecting a uniaxial loadcell with higher load capacity

could increase the load capacity and sensitivity. For Gen 1.0, loadcells along the z-axis had higher load capacities (i.e., 100 kg) since these loadcells carried higher loads due to the subject's weight (Table I). The loadcells along the x, y-axis had smaller load capacities (i.e., 20 kg, 30 kg), but higher sensitivities since the expected loads along these directions were smaller in magnitude. There was a greater number of loadcells along the z-axis (n=3) than x- or y-axis (n=2 for x-axis, n=1 for y-axis) for similar reasons. For Gen 2.0, all loadcells had identical load capacities (i.e., 100 kg) since all loadcells shared approximately similar loads due to the symmetric loadcell arrangement. Versatility and guidelines for FSS design are further discussed in the GitHub link.

b) Construction of FSS

Both the FSS Gen 1.0 and 2.0 shared the same core design principle (i.e., force-torque sensor consisting of a base, plate, and six strategically arranged legs) but had key differences in terms of construction materials and manufacturing/assembly methods. The FSS Gen 1.0 was manually fabricated using readily available materials such as medium density fiber (MDF) boards and aluminum extrusions. The FSS Gen 2.0 was more precisely fabricated by water-jetting sheets of 7075-T6 aluminum for the plate (Figure 3). Extrusions of 6105-T5 aluminum were used for the base.

c) Cost-effective Electrical Design of FSS

For both FSS designs, commercially available low-cost uniaxial loadcells and loadcell amplifiers were chosen. FSS 1.0 utilized six loadcells (DYMH-103, Calt, China) with different load capacities depending on the axis (X-axis: 20 kg, Y-axis: 30 kg, Z-axis: 100 kg) with six identical amplifiers (NAU7802, Nuvoton, Taiwan). FSS 2.0 used six identical load cells (CZL301C, Hualanhai, China) with three dualamplifiers (ABE-01, Robotshop, Canada). Since these loadcells and their amplifiers were mostly hobby-grade, we verified each loadcell's performance. Loads from 0 to 75% of the loadcell's load capacity (at increments of 20 N) were added to one end of a leg while the other end of the leg was fixed. The loadcell readings and the actual load value were compared to analyze the performance (i.e., hysteresis, nonlinearity, zero output [15]) of each loadcell. The performance results demonstrated that the chosen loadcells and amplifiers were sufficiently accurate and repeatable to be used for PURE's application. The empirically measured values of the hysteresis, load capacity, non-linearity, and zero output for the loadcells in FSS 1.0 and 2.0 were all within 0.05% of the reported values.

The overall FSS electrical system consisted of a microcontroller (Teensy 4.1, PJRC, USA) and loadcell amplifiers for both FSS 1.0 and 2.0. The loadcell data along with a time stamp and IMU data were transmitted to and recorded on a PC via micro-USB cable at 100 Hz. For both FSSs, the amplifier's gains were tuned to ensure that the loadcell's maximum capacity could be reached without saturation. The amplifier's zero-offsets were also adjusted to ensure the loadcell's bidirectionality (i.e., ability to measure loads in tension and compression equally), respectively. For FSS Gen 1.0, the chosen loadcell amplifier provided

programmable gains and sampling rates, higher resolution, and a built-in filter for rejecting 50 Hz and 60Hz noise due to electric humming. The amplifiers all had identical and unchangeable i2c addresses, so a multiplexer (TCA9548A, Texas Ins., USA) was added to enable reading of multiple loadcell amplifier simultaneously. For FSS Gen 2.0, a different loadcell amplifier that communicated directly to the microcontroller via analog signal was selected to 1) sample the loadcell signals at higher frequency (400 Hz) for future PURE development, and 2) simplify the electrical system by removing the multiplexer. For an electrical diagram, refer to the GitHub link.

2) Inertial Measurement Unit (IMU)

The IMU aimed to estimate the kinematic signals of the rider's torso motion. The IMU was attached to the subject's manubrium since it offered a flat and accessible surface for the IMU to be placed on for both male and female riders. A commercially available industrial grade 9-axis IMU was used since it was a small $(35\text{mm} \times 33\text{mm} \times 9\text{mm})$ and light (0.15kg) wearable device. The IMU quantified the 3D torso angles in terms of 3D intrinsic Euler Angles in "XYZ" order such that the yaw (θ_{yaw}^{IMU}) , pitch (θ_{pitch}^{IMU}) , and roll (θ_{roll}^{IMU}) represented the motions of torso twisting, leaning anterior/posterior, and leaning laterally/medially, respectively (Figure 2). The desired estimation requirements of the IMU were a range of -180° to 180° and accuracy of 6°. Other studies defined a 6° as the maximum allowable root-meanssquared error (RMSE) for accurately estimating human joint angles [16]. The 3D angles from the IMU were recorded by a microcontroller at 100 Hz. A transceiver (MAX3232, Texas Ins., USA) was used to convert the RS-232 signals (-5V to +5V) from the IMU to TTL signals (-3.3V to 5V) for the microcontroller.

An on-board proprietary algorithm based on Extended Kalman Filter was utilized to compute the 3D Euler Angles (VN-100, VectorNav, USA). The algorithm utilized the integration of the 3-axis gyroscopic readings to provide faster and smoother estimates of 3D Euler Angles. Gyroscopes are subjected to bias instabilities, however, causing the integration of the gyroscopic readings to drift over time due to the inherent noise properties (e.g., gyro bias) of the gyroscope [16]. Thus, the algorithm used the accelerometer and magnetometer measurements to continuously estimate the gyro bias and compensate for this drift. The algorithm relied on the 3-axis accelerometers to estimate the direction of gravity, serving as reference for determining θ_{pitch}^{IMU} and θ_{roll}^{IMU} . Similarly, the 3-axis magnetometers were used to estimate the direction of the Earth's magnetic field, serving as a reference for computing θ_{vaw}^{IMU} .

The IMU was set to use the Relative Heading Mode (RHM), i.e., a selectable mode offered by the chosen IMU model, in which the dependence on the magnetometer readings was reduced for computing the 3D angles to reject magnetic disturbances in an indoor environment [17]. The RHM allowed more stable computation of relative θ_{yaw}^{IMU} (= 0 at the start-up of the IMU) resistant to nearby magnetic disturbances at the expense of computing absolute θ_{yaw}^{IMU} (= 0 when the IMU was aligned to the Earth's magnetic North).

This was done by using only the minimal information from the magnetometer data to correct for the gyroscopic bias and drift behavior. The algorithm constantly monitored the stability of the magnetic field and maintained stable θ_{yaw}^{IMU} if the surrounding magnetic field was stable. While RHM could not compute absolute θ_{yaw}^{IMU} , RHM was suitable for our study since 1) computing the relative θ_{yaw}^{IMU} , rather than absolute θ_{yaw}^{IMU} , was sufficient for achieving the HF control of PURE, and 2) magnetic disturbance rejection was critical since PURE was mostly used indoors where magnetometers are often unreliable [18].

B. TES Validation

A convenience sample of eight gender-matched ablebodied users (ABUs, 3F:3M, 26.8±1.5 yrs, 61.6±11.0 kg, 1.7±0.1 m) and manual wheelchair users (mWCUs, 1F:1M, 20.5±2.1 yrs, 55.7±17.3 kg, 1.5±0.0 m, 17.5±2.5 yrs of mWC) were recruited to perform trials to verify if the TES could accurately quantify torso motions. Rather than asking ablebodied subjects to also perform motions with reduced range of motion, mWCUs were included to assess their smaller and less dynamic torso motions and potentially unique movement patterns, especially since PURE is intended for use by mWCUs. The same subjects were used in the validation for FSS Gen 1.0 and 2.0. Subjects provided informed consent and the experimental protocol was approved by the Institutional Review Board of the University of Illinois at Urbana-Champaign (IRB 22552).

The estimations of the kinetic values from the FSS were compared to a research grade force plate, and the kinematic values from the IMU were compared to a research grade 6camera motion capture system (Ogus 500, Oualisys, Sweden) to ensure accurate estimations (Figure 2). Due to the design differences, two test setups were used for validating the FSS Gen 1.0 and Gen 2.0 devices. Both consisted of the FSS being firmly secured on top of the force plate using clamps. The setup for FSS Gen 1.0 used an elevated testing plate to raise the force plate (BP600900-1K, AMTI, USA) and FSS up to a comfortable height for the test subjects to get seated easily and safely. The test setup for FSS Gen 2.0 required the use of a smaller force plate (OR6-7-2000, AMTI, USA) than for FSS Gen 1.0 to better secure the FSS Gen 2.0 to the force plate. An L-shaped frame with four motion markers was placed on the force plate and parallel to the force plate's coordinate system to align the MoCap and force plate systems. Each FSS had four motion markers, one placed on each corner of the seat, to record the position and orientation of the seat's center using the MoCap system. A small 3D printed module that served as the base for the IMU and three motion markers was made to ensure 1) that the IMU and MoCap were reading the dynamics of the same moving body, and 2) consistent placement of the IMU and markers relative to each other for all subjects (Figure 2). The three markers established a reference frame for the subject's torso, enabling the formulation of a rotation matrix, which was used to compute the ground truth 3-D torso angles $(\theta_{yaw}^{MoCap}, \theta_{pitch}^{MoCap}, \theta_{roll}^{MoCap})$ [19]. The module was secured on the subject's manubrium using medical-grade double-sided adhesive tape.

The seat was adjusted to each subject's preference, and the subject was prepared and seated on the FSS. The FSS seat depth, dump angle, backrest height, and footrest positions were adjusted for each subject following ergonomic guidelines [20]. Each subject wore an open-neck T-shirt and shoes and was instructed to sit in a neutral position (i.e., sitting centered along y-axis (left/right direction of the FSS), hands placed on laps, elbows tucked into torso, 90° bends in hips, knees, and ankles, and head facing forward) (Figure 4 (1)).

The physical FSSs had dimensional inaccuracies due to tolerance errors from manufacturing and assembly. These discrepancies between the ideal and actual dimensions would be reflected in the force transformation matrix H, causing inaccurate calculations of the externally applied wrenches. A calibration procedure can greatly improve the accuracy of the FSS estimations by correcting for tolerance errors [14]. The single subject, whose data were used to create Table 1, performed a series of predefined torso movements (Figure 4), while data from the force plate and the FSS were collected from the Gen 1.0 and 2.0 test setups. The collected calibration data were utilized to derive an error matrix for each device, which found the best fit between a series of ground truth data from the force plate and the estimated un-calibrated wrench data from the FSS using a least squared method [14]. The mathematical details of calibration are explained in the GitHub link. The calibration was performed only once for each version of the FSS.

For the validation assessments, each subject performed two sets of trials, one for each FSS test setup. For each set, the subject performed ten predefined torso movements that mimicked rider movements on PURE (Figure 4). For each torso movement, the subject was instructed to move their torso at a comfortable range of motion. A metronome set to 70 bpm was used to provide an audible cue for the subject to maintain consistent movement speed (35°/s). Each movement was repeated four times. The order of the test sets was randomized for each subject. During each trial, the following data were collected at 100Hz: time stamp, 3D positions of 11 markers (IMU module, FSS surface, L-frame), six FSS loadcell readings ($f_1, f_2 \dots f_6$), three IMU readings ($\theta_{yaw}^{IMU}, \theta_{pitch}^{IMU}, \theta_{roll}^{IMU}$), and force plate measurements $(\overline{\mathbf{F}}_A, \overline{\mathbf{T}}_A, \overline{\mathbf{COP}}_A)$. The loadcell readings were used to compute the FSS torso kinetic movement metrics $(\vec{F}_x, \vec{F}_y, \vec{F}_z, \vec{T}_x, \vec{T}_y, \vec{T}_z)$ COP_{x} , COP_{y}).

To assess the accuracy of the estimations of the FSS and IMU, a total of 11 RMSE values between the measurements from the TES and the research grade equipment were examined [21]. For the FSS, the allowable average RMSE values are presented in Table 1. For the IMU, the allowable RMSE values were 6° for all three Euler angles.

III. RESULTS

The FSS devices were able to collect kinetic data applied to the seat across a range of movements performed by the test subjects (Figure 5). Some signals such as COP_x fluctuated sinusoidally while other signals (e.g., \vec{F}_z) remained relatively constant. The magnitude of kinetic signals of ABUs were generally larger than mWCUs, as expected. The FSS Gen 1.0

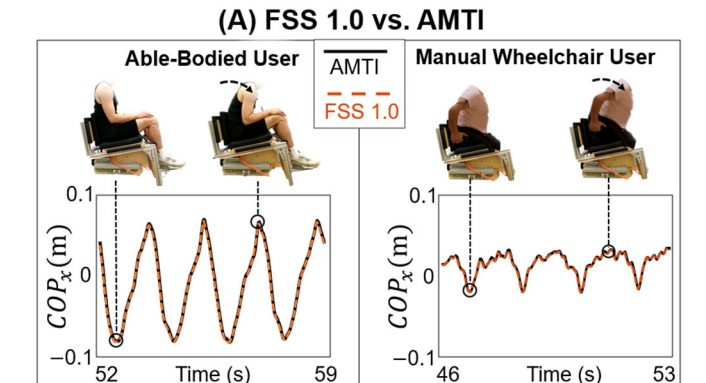


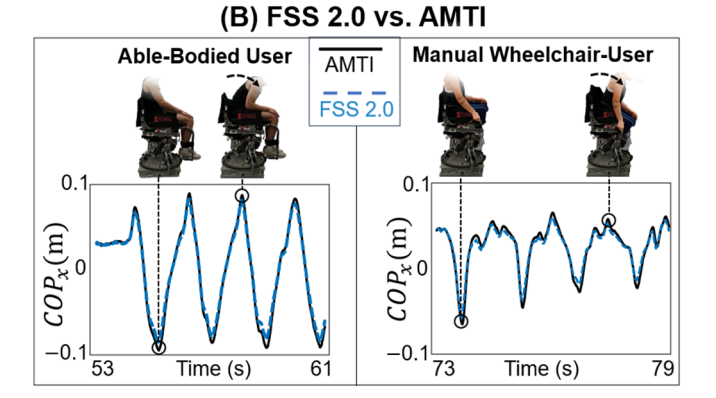
Figure 4. Subjects performed a series of torso movements starting with (1) neutral position, (2) leaning forward/backwards, (3) leaning left/right, (4) leaning diagonal left/right, (5) twisting, (6) leaning forward + twisting, (7) leaning left + twisting, (8) leaning right + twisting, (9) leaning diagonally left + twisting, and (10) leaning diagonally right + twisting.

estimations of torso motions displayed low RMSEs compared to the force plate satisfying the desired design specifications across all test subjects (Table 1,2). Average RMSE of 3D forces, 3D torques, 2D COP, and torso angles were generally larger than mWCUs, as expected. The FSS Gen 1.0 estimations of torso motions displayed low RMSEs compared to the force plate satisfying the desired design specifications across all test subjects (Table 1,2). Average RMSE of 3D forces, 3D torques, and 2D COP were about 2.7 N, 0.9 Nm, 1.2 mm, respectively. There was no difference in RMSE of kinetic signals among ABUs and mWCUs. The differences of the RMSEs between ABUs and mWCUs were less than 1 N, 0.5 Nm, and 0.2 mm for the forces, torques, and COPs, respectively. Thus, the estimations of FSS Gen 1.0 showed good accuracy in different directions and ranges of magnitudes for different users.

The FSS Gen 2.0 estimations of torso motions exhibited low RMSEs for all subjects while satisfying the desired targets (Table 2, Figure 5). Average RMSE of 3D forces, 3D torques, and 2D COP were approximately 8.6 N, 2.5 Nm, 3.1 mm, respectively. The FSS Gen 2.0 demonstrated slightly less accuracy for different directions (i.e., less isotropic accuracy) and ranges of magnitudes (i.e., less invariant to applied load magnitudes) than FSS Gen 1.0. The RMSE for $\vec{\mathbf{F}}_z$ was slightly higher than the $\vec{\mathbf{F}}_{x}$, $\vec{\mathbf{F}}_{v}$ that experienced only small force magnitudes. The RMSE for $\overline{\mathbf{T}}_{v}$ was slightly higher by 1.5 Nm than for \vec{T}_x and \vec{T}_z . The RMSE for COP_x was slightly higher by 0.75 mm than for COP_y . Also, the standard error of the RMSEs for FSS Gen 2.0 were slightly higher by 1.4 N, 0.8 Nm, and 0.9 mm for the forces, torques, and COPs, respectively. Like FSS Gen 1.0, the FSS Gen 2.0 RMSEs were similar between ABUs and mWCUs. The differences of the RMSEs between ABUs and mWCUs were less than 3 N, 1.5 Nm, and 2 mm for the forces, torques, and COPs, respectively.

The IMU estimations exhibited low RMSE for quantifying torso motions for ABUs and mWCUs, satisfying PURE's design requirement (Table 2). All three angles from the IMU displayed RMSE less than 6°, the maximum allowable RMSE for quantifying human joint angles. The IMU's yaw angle





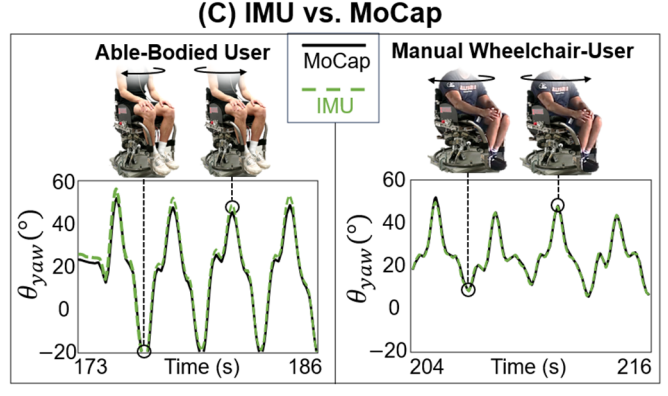


Figure 5. Representative plots of COP_x from (a) FSS Gen 1.0 and (b) FSS Gen 2.0 compared to the AMTI force plate for an able-bodied user (ABU, S6, Female) and manual wheelchair user (mWCU, S8, Male) during torso leaning forward and back to neutral position. (c) Representive plots of θ_{yaw} of IMU compared to motion capture (MoCap) for the same ABU and mWCU. Other measurements (i.e., \vec{F} , \vec{T} , COP_y , θ_{roll} , θ_{pitch}) of the FSS Gen 1.0, 2.0, and IMU displayed similar levels of accuracy.

demonstrated no significant drifting behavior for all subjects (RMSE < 4°). The IMU's pitch and roll angle displayed higher accuracy (RMSE < 2°) than the yaw angle for ABUs and mWCUs, who exhibited smaller ROM about the pitch axis. The RMSE for pitch and roll angles for mWCUs were smaller (sometimes < 1°) than ABUs.

I. DISCUSSION

The Torso-dynamics Estimation System (TES), consisting of a Force Sensing Seat (FSS) and an inertial measurement unit (IMU), can accurately quantify torso motions of ablebodied users (ABUs) and manual wheelchair users (mWCUs) for the HF control of PURE.

The two versions of the FSS demonstrated sufficient accuracy, fulfilling the desired accuracy in Table 1. They accurately estimated the kinetic signals of the subject's torso motions while satisfying the spatial and inertial design criteria. Both FSS versions estimated the 3D forces, 3D torques, and 2D COPs with high accuracy while satisfying the spatial and inertial design requirements. Both versions of the FSS were sufficiently sensitive and could quantify the small torso motions of mWCUs as well as the large torso motions of ABUs since the accuracy of FSSs did not change significantly for both user groups.

The two FSS designs displayed high versatility in design and construction method while utilizing cost-effective components. Even though the two FSSs differed in terms of the loadcell layout (e.g., orthogonal vs. Stewart platform), manufacturing method (e.g., manual drilling vs. water jetting), and materials (e.g., MDF vs. aluminum plates), only slight differences of accuracies were observed in terms of the accuracies. For example, the FSS Gen 1.0 RMSEs for COP_x and COP_v were only different by 3-5 mm compared to FSS Gen 2.0. The FSS design offered a cost-efficient solution for accurately estimating kinetic signals. Both FSS designs exhibited high accuracy albeit the use of low-cost loadcell components (< \$75 per loadcell) and amplifiers (< \$20 per amplifier). Commercially available multi-axis (and even single-axis) force-torque sensors can be costly (> \$4,000 for multi-axis, > \$1,000 for single-axis) [22].

The sources of error for both FSSs could be attributed to the inherent mechanical compliance in the system and inaccuracy of the individual loadcell measurement. The compliance could originate from any elastic bending of various mechanical components (e.g., plate) as well as the mechanical interfaces between components (e.g., interface between rod ends and fasteners). These compliances would violate the assumption (i.e., rigid mechanical system) for computing forces and torques, causing H to become a variant matrix, and ultimately introducing errors for the FSS estimations. Other studies pointed out the drawbacks of rodends such as potential sources of error due to backlashes from the clearance at the joints [11], [14]. This mechanical compliance could also explain why FSS Gen 1.0 exhibited slightly higher accuracy than Gen 2.0. The lower accuracy of FSS 2.0 can be attributed to the larger mechanical compliance introduced due to a larger offset created by the support structure and drive train (Figure 2). This large offset between the base of FSS Gen 2.0 and the top surface of AMTI force plate allowed larger elastic deformations to occur since the large offset acted as a longer lever arm which amplified the loads experienced by the system. Thus, the assumptions for calculating FSS Gen 2.0 signals were violated more severely than the FSS Gen 1.0, introducing higher error for estimation of FSS Gen 2.0 signals were violated more severely than the FSS Gen 1.0, introducing higher error for estimation of FSS Gen 2.0 signals. However, despite the differences of accuracies between the two FSSs, both FSS versions were sufficiently accurate, sensitive, versatile, and practical to be used for HF control of mobile robots such as PURE.

The IMU accurately estimated the 3D angles of torso (Table 2). The yaw, pitch, and roll angles from the IMU were

TABLE 2. ACCURACY OF FSS GEN 1.0 & 2.0 AND IMU FOR ABLE-BODIED USERS (ABUS) & MANUAL WHEELCHAIR USERS (MWCUS)

	C DEAD (FSS G		ALE WHEN	FSS Gen 2.0				
	ABU		mWCU		ABU		mWCU		
	RMSE	[min, max]	RMSE	[min, max]	RMSE	[min, max]	RMSE	[min, max]	
F _x (N)	2.2	[-83.0,	1.7	[-106.0,	8.7	[-40.0,	5.1	[-23.3,	
	a(0.9)	63.4]	(0.9)	102.0]	(2.4)	27.2]	(2.8)	6.2]	
$\vec{\mathbf{F}}_{y}$ (N)	3.8	[-52.1,	3.7	[-91.1,	7.1	[-20.0,	7.7	[-3.3,	
	(1.4)	57.8]	(3.3)	77.0]	(1.2)	51.1]	(1.9)	43.0]	
$\vec{\mathbf{F}}_{\mathbf{z}}$ (N)	2.5	[453.5,	2.2	[425.6,	12.6	[395.2,	10.1	[399.4,	
	(0.4)	792.3]	(0.8)	799.0]	(1.2)	857.9]	(2.3)	682.7]	
\vec{T}_x (Nm)	0.9	[-91.9,	0.7	[-77.3,	2.7	[-88.1,	2.5	[-66.8,	
	(0.3)	87.6]	(0.4)	66.9]	(0.4)	108.1]	(1.4)	68.9]	
$\overrightarrow{\mathbf{T}}_{y}$ (Nm)	0.8	[-80.0,	0.9	[50.1,	4.0	[-99.6,	2.6	[-28.9,	
	(0.3)	87.6]	(0.6)	89.2]	(1.0)	200.0]	(1.6)	78.7]	
$\overrightarrow{\textbf{T}}_z\\(\text{Nm})$	1.1	[-24.7,	0.7	[-33.7,	1.5	[-25.0,	1.7	[-2.1,	
	(0.4)	18.3]	(0.3)	14.2]	(0.4)	53.8]	(1.2)	14.2]	
<i>COP_x</i> (mm)	1.1	[-189.2,	1.3	[-158.6,	6.0	[-313.7,	4.1	[-125.1,	
	(0.3)	102.4]	(0.7)	74.2]	(1.5)	131.4]	(1.8)	44.4]	
COP _y (mm)	1.3	[-118.0,	1.1	[-111.5,	4.5	[-129.7,	4.0	[-107.7,	
	(0.3)	113.6]	(0.1)	98.0]	(1.0)	168.7]	(1.8)	104.6]	
$ heta_{yaw}^{IMU}$ (°)	2.5	[-57.3,	3.1	[-40.4,	1.6	[-63.9,	1.3	[-51.9,	
	(1.0)	61.1]	(2.4)	51.6]	(0.4)	58.1]	(0.7)	55.1]	
$ heta_{pitch}^{IMU}$ (°)	1.1 (0.3)	[-53.5, 40.2]	0.8 (0.5)	[-26.0, 9.5]	1.3 (0.6)	[-45.7, 44.4]	0.8 (0.4)	[-21.0, 17.3]	
$ heta_{yaw}^{IMU}$ (°)	2.5	[-34.8,	3.1	[-24.9,	1.6	[-34.5,	1.3	[-31.0,	
	(1.0)	37.3]	(2.4)	59.4]	(0.4)	34.4]	(0.7)	38.2]	

^aStandard Errors from TES (in parentheses)

all accurate (RMSE < 6°) and sensitive to quantify small torso motions of mWCUs to large torso motions of ABUs. The yaw angle computation from the IMU was sufficiently accurate (RMSE < 4°) for commanding the spin motion of the PURE. The pitch and roll computation from the IMU were even more accurate (RMSE < 3°). Unlike the yaw angle calculation that has no reference vectors, the calculation of the pitch and roll can rely on using gravity as reference, enabling the computation of more accurate and drift-free angles.

While the computation of IMU angles were accurate, there were some practical issues regarding the setup and use of the IMU. On rare occasions the IMU's yaw angle would start immediately drifting upon start-up of the IMU. It was important to wait until a stable yaw angle was achieved. In the scenario when the IMU's yaw angle did not stabilize, a power cycle of the IMU was necessary. Since the IMU algorithm was proprietary, it was unclear what the cause for this random drifting behavior was. However, this undesirable behavior did not occur often, and the IMU was simply rebooted when the behavior did occur.

A few limitations were observed in this study. First, the sample size was small. More participants with different physiques would enable us to assess if TES estimations remain accurate for broader user groups. Second, the TES was

not tested in dynamic test conditions. These conditions may include tilting and acceleration/deceleration of the device to better simulate the loads experienced during riding of the PURE. The simulation of these loads can be done by installing the FSS test setup on top of a controllable moving plate (e.g., active Stewart platform) that can tilt and replicate loads in 3D. However, the accuracy of the FSSs will not likely be affected by these additional loads since the FSS model is mostly invariant to the magnitude and direction of loads.

The design of the TES can be iterated to further improve its accuracy, versatility in design, as well as user experience. The FSS can incorporate preloads to remove the compliance in the mechanical components, increasing the accuracy of the FSS. The preloads can be applied in various ways such as creating a hyper-static structure by adding a spring-loaded seventh leg vertically [11]. The FSS can also utilize custom loadcells to provide more versatility in design [10], [12], [14]. The IMU, a wearable solution, may be replaced by other solutions (e.g., a computer vision system estimating the user's 3D pose [23]) to remove the need for the user to wear a device.

II. CONCLUSION

A Torso-dynamics Estimation System, i.e., Force Sensing Seat and Inertial Measurement Unit, was developed to quantify the torso motions of able-bodied users and manual wheelchair users in terms of kinetic and kinematic signals. The FSS utilized six strategically arranged loadcells to compute kinetic signals generated by the user's torso motion (i.e., 3D forces, 3D torques, 2D COPs). Two versions of the FSS were developed with varying loadcell arrangement, construction materials, fabrication, and assembly methods. An algorithm using an industrial grade IMU with minimal reliance on magnetometers was used to compute the 3D kinematic torso angles. Both versions of the FSS and IMU provided sufficiently accurate and sensitive estimations of the kinetic and kinematic signals, while satisfying strict spatial and inertial design criteria. The TES can have many applications such as teleoperation or remote control of virtual mobile robots and locomotion.

ACKNOWLEDGMENT

We thank Professor Deana McDonagh, Professor William Norris, Doctor Patricia Malik, and Shayna Talpallikar for their assistance to the project, and Virgil Ward of Grainger College of Engineering Marketing and Communication Group for taking PURE's photos and videos.

REFERENCES

- [1] Y. Chen, D. Paez Granados, H. Kadone, and K. Suzuki, 'Control Interface for Hands-free Navigation of Standing Mobility Vehicles based on Upper-Body Natural Movements', 2020 IEEE/RSJ International Conference on Intelligent Robots and Systems (IROS), Las Vegas, NV, USA, pp. 11322-11329, 2020, doi: 10.1109/IROS45743.2020.9340875.
- [2] E. B. Thorp et al., 'Upper Body-Based Power Wheelchair Control Interface for Individuals With Tetraplegia', IEEE Transactions on Neural Systems and Rehabilitation Engineering, vol. 24, no. 2, pp. 249– 260, Feb. 2016, doi: 10.1109/TNSRE.2015.2439240.
- [3] M. Jenifer et al., 'Data-driven body-machine interface for the accurate control of drones', Proceedings of the National Academy of Sciences,

- vol. 115, no. 31, pp. 7913–7918, Jul. 2018, doi: 10.1073/pnas.1718648115.
- [4] J. Hori, H. Ohara, and S. Inayoshi, 'Control of speed and direction of electric wheelchair using seat pressure mapping', *Biocybernetics and Biomedical Engineering*, vol. 38, no. 3, pp. 624–633, 2018, doi: 10.1016/j.bbe.2018.04.007.
- [5] M. Macchini, F. Schiano, and D. Floreano, 'Personalized Telerobotics by Fast Machine Learning of Body-Machine Interfaces', *IEEE Robotics* and Automation Letters, vol. 5, no. 1, pp. 179–186, 2020, doi: 10.1109/LRA.2019.2950816.
- [6] C. Rognon, S. Mintchev, F. Dell'Agnola, A. Cherpillod, D. Atienza, and D. Floreano, 'FlyJacket: An Upper Body Soft Exoskeleton for Immersive Drone Control', *IEEE Robotics and Automation Letters*, vol. 3, no. 3, pp. 2362–2369, 2018, doi: 10.1109/LRA.2018.2810955.
- [7] R. Eguchi and M. Takahashi, 'Validity of the Nintendo Wii Balance Board for Kinetic Gait Analysis', *Applied Sciences*, vol. 8, no. 2, 2018, doi: 10.3390/app8020285.
- [8] R. A. Clark, B. F. Mentiplay, Y.-H. Pua, and K. J. Bower, 'Reliability and validity of the Wii Balance Board for assessment of standing balance: A systematic review', *Gait & Posture*, vol. 61, pp. 40–54, 2018, doi: 10.1016/j.gaitpost.2017.12.022.
- [9] Y. Kwon, 'Center of pressure (GRF application point)', 1998. http://www.kwon3d.com/theory/grf/cop.html (accessed Mar. 02, 2023).
- [10] R. Ranganath, P. S. Nair, T. S. Mruthyunjaya, and A. Ghosal, 'A force-torque sensor based on a Stewart Platform in a near-singular configuration', *Mechanism and Machine Theory*, vol. 39, no. 9, pp. 971–998, 2004, doi: 10.1016/j.mechmachtheory.2004.04.005.
- [11]Z. Wang, Z. Li, J. He, J. Yao, and Y. Zhao, 'Optimal design and experiment research of a fully pre-stressed six-axis force/torque sensor', *Measurement*, vol. 46, no. 6, pp. 2013–2021, 2013, doi: 10.1016/j.measurement.2013.03.003.
- [12] T. A. Dwarakanath and D. Venkatesh, 'Simply supported, "Joint less" parallel mechanism based force-torque sensor', *Mechatronics*, vol. 16, no. 9, pp. 565–575, 2006, doi: 10.1016/j.mechatronics.2006.03.013.
- [13] J. Yao, Y. Hou, H. Wang, T. Zhou, and Y. Zhao, 'Spatially isotropic configuration of Stewart platform-based force sensor', *Mechanism and Machine Theory*, vol. 46, no. 2, pp. 142–155, 2011, doi: 10.1016/j.mechmachtheory.2010.10.002.
- [14] T. A. Dwarakanath and G. Bhutani, 'Beam type hexapod structure based six component force-torque sensor', *Mechatronics*, vol. 21, no. 8, pp. 1279–1287, 2011, doi: 10.1016/j.mechatronics.2011.08.004.
- [15] 'What is Load Cell Accuracy', Futek. https://www.futek.com/load-cell-accuracy (accessed Dec. 01, 2022).
- [16]T. Seel, J. Raisch, and T. Schauer, 'IMU-Based Joint Angle Measurement for Gait Analysis', Sensors, vol. 14, no. 4. 2014. doi: 10.3390/s140406891.
- [17] W. H. K. de Vries, H. E. J. Veeger, C. T. M. Baten, and F. C. T. van der Helm, 'Magnetic distortion in motion labs, implications for validating inertial magnetic sensors', *Gait & Posture*, vol. 29, no. 4, pp. 535–541, 2009, doi: 10.1016/j.gaitpost.2008.12.004.
- [18] M. El-Gohary and J. McNames, 'Human Joint Angle Estimation with Inertial Sensors and Validation with A Robot Arm', *IEEE Transactions* on *Biomedical Engineering*, vol. 62, no. 7, pp. 1759–1767, 2015, doi: 10.1109/TBME.2015.2403368.
- [19] J. Diebel, 'Representing attitude: Euler angles, unit quaternions, and rotation vectors', *Matrix*, vol. 58, no. 15–16, pp. 1–35, 2006.
- [20] R. A. Cooper, 'Engineering manual and electric powered wheelchairs.', Critical reviews in biomedical engineering, vol. 27, no. 1–2, pp. 27–73, 1999, doi: 10.1615/critrevbiomedeng.v27.i1-2.20.
- [21] T. Chai and R. R. Draxler, 'Root mean square error (RMSE) or mean absolute error (MAE)? Arguments against avoiding RMSE in the literature', Geoscientific Model Development, vol. 7, no. 3, pp. 1247– 1250, 2014.
- [22] R. P. Ubeda, S. C. Gutiérrez Rubert, R. Zotovic Stanisic, and Á. Perles Ivars, 'Design and manufacturing of an ultra-low-cost custom torque sensor for robotics', *Sensors*, vol. 18, no. 6, p. 1786, 2018.
- [23] D. Mehta et al., 'VNect: Real-Time 3D Human Pose Estimation with a Single RGB Camera', ACM Trans. Graph., vol. 36, no. 4, Jul. 2017, doi: 10.1145/3072959.3073596.
- ^a https://github.com/ssong47/TorsodynamicsEstimationSystem.git